Multiorbital physics in Fermi liquids prone to magnetic order

Malte Behrmann, Christoph Piefke, and Frank Lechermann
I. Institut für Theoretische Physik, Universität Hamburg, D-20355 Hamburg, Germany
(Received 14 March 2012; published 26 July 2012)

The interplay of spin-orbit coupling and strong electronic correlations is studied for the single-layer and the bilayer compound of the strontium ruthenate Ruddlesden-Popper series by a combination of first-principles band-structure theory with mean-field rotationally invariant slave bosons. At equilibrium strongly renormalized (spin-orbit-split) quasiparticle bands are traced and a thorough description of the low-energy regime for the nearly ferromagnetic bilayer system in accordance with experimental data is presented. The metamagnetic response of $Sr_3Ru_2O_7$ in finite magnetic field H is verified and a detailed analysis of the underlying correlated electronic structure provided. Intriguing multiorbital physics on both local and itinerant level, such as competing paramagnetic and diamagnetic contributions, is observed with important differences depending on the magnetic-field angle θ with the crystallographic c axis.

DOI: 10.1103/PhysRevB.86.045130 PACS number(s): 71.27.+a, 71.18.+y, 75.10.Lp, 75.70.Tj

I. INTRODUCTION

Ternary ruthenium-based oxide compounds condense in a rich variety of different crystal-structure types with associated rather delicate electronic and magnetic properties.[1] Within the perovskite-like Ruddlesden-Popper series of the ruthenates $A_{n+1}Ru_nO_{3n+1}$ (A =Sr, Ca), where n labels the layers of corner-sharing RuO_6 octahedra (separated by SrO or CaO rocksalt layers), the interacting electrons pose a specifically challenging problem. In that family of seemingly rather similar compounds, intriguing competitions between Fermi-liquid, Mott-insulating, and superconducting behavior occur in conjunction with particular complex magnetic response. For instance, albeit Ca and Sr are isovalent, the respective single-layer compounds A_2RuO_4 exhibit drastically different phenomenology, since Sr_2RuO_4 displays unconventional superconductivity below $T_c \sim 1.5$ K,[2–4] while Ca_2RuO_4 becomes an antiferromagnetic (AFM) Mott insulator below $T_{MI} \sim 77$ K.[5,6] As an important generic distinction, compared to the Sr compounds the Ca subclass in the series exhibits stronger distortions and deviations from an ideal high crystal symmetry.

A prominent aspect of the intricate physics in the overall metallic strontium ruthenates is the onset of ferromagnetism with n. Concerning the series end members, the perovskite $SrRuO_3$ ($n \to \infty$) is ferromagnetic (FM) below $T_c \sim 165$ K and tetragonal Sr_2RuO_4 ($n = 1$) is paramagnetic (PM) at ambient temperature T, but shows FM tendencies as well as incommensurate spin fluctuations at $\mathbf{q} = (\pm 0.6\pi/a, \pm 0.6\pi/a, 0)$.[7,8] The ($n = 3$) $Sr_4Ru_3O_{10}$ and the ($n = 2$) $Sr_3Ru_2O_7$ compounds are both orthorhombic, but whereas the former is verified FM,[9] the latter is still PM down to low temperatures. However the bilayer system appears to be located rather close to the transition towards FM order,[10] with puzzling metamagnetic (MM) behavior in applied field below $T_{MM} \sim 1$ K (see Ref. 11 for a recent review). As revealed from de Haas–van Alphen (dHvA),[12] angle-resolved photoemission spectroscopy (ARPES),[13–16] optics,[17] and resistivity[10] measurements, the $n = 1,2$ compounds (see Fig. 1) both belong to cases of quasi-two-dimensional (2D) electron systems, i.e., show a strong anisotropy between transport in the ab plane and along the c axis of the crystal structure. Signatures of strong electronic correlations are compelling for these layered ruthenates, e.g., from large mass renormalizations,[10,18,19] and originate from the less-screened Coulomb interactions within the Ru($4d$) shell. Nominally four electrons occupy this $l = 2$ manifold; i.e., an Ru^{4+} oxidation state may be assumed. The metamagnetism with applied field H in $Sr_3Ru_2O_7$ is well documented by a large slope $\frac{\partial M}{\partial H}|_{H_{MM}}$ around $H_{MM} = 5.5(7.7)$ T for $H||ab(c)$.[20,21] Furthermore this MM region may be associated with being in the neighborhood of a quantum-critial point that can be approached via tuning the polar angle θ between magnetic field and the c axis.[22,23] Reachable within fields $H < 10$ T, the MM phenomena are acting on a very low energy scale of the order of at most a few meV. In this respect, the Fermi-liquid regime in vanishing field exists below 10–15 K, however can be driven to zero temperature with applied field.[24]

In this work we present a theoretical investigation of the $n = 1,2$ compounds in the normal state of the low-temperature regime with an emphasis on the intriguing physics of the bilayer system in applied magnetic field. The study is based on the combination of a first-principles band-structure approach, spin-orbit-interaction treatment in the Russell-Saunders limit, and mean-field many-body theory. The peculiar low-energy physics of the layered ruthenates ask for a very detailed examination of the single- and many-particle terms in the Hamiltonian in order to capture the important processes that drive the physics of these systems.[3,7,16,25–47] Besides the thorough description of the crystal bonding which leads to a multiorbital-based band manifold at the Fermi level, it was shown[28,30,32] that additionally spin-orbit effects play a vital role in the low-energy regime. Focusing on the many-body part, e.g., the relevance of the Hund's coupling J_H in addition to the larger Hubbard U was elucidated in several works.[25,27,31] Much theoretical effort has also been devoted to the description of the MM phenomena in $Sr_3Ru_2O_7$, either based on effective single-band modelings[35–39,44] or with including multiband degrees of freedom.[40–43,45] The existing model studies are able to account for the principle appearance of metamagnetism, often accompanied by nematic order,[37] i.e., broken rotational symmetry. Important ingredients for the MM behavior are van Hove singularities close to the Fermi surface, already

revealed in the single-band approaches.[35] More sophisticated multiorbital investigations have been employed to discriminate between the importance of d_{xz}, d_{yz} (formally quasi-1D-like dispersions) and d_{xy} (formally quasi-2D-like dispersions) orbital degrees of freedom together with spin-orbit coupling (SOC). However often the broken fourfold symmetry in $Sr_3Ru_2O_7$ is neglected, when modeling the electronic states. In addition, most theoretical works treat the many-body interactions in the Hartree-Fock approximation, not allowing for explicit self-consistent renormalizations and ill defined for the metallic regime.

A combination of the local density approximation (LDA) to density functional theory (DFT) with slave-boson[48–51] theory in a rotationally invariant representation[52,53] was utilized in Ref. 46 in order to account for renormalized quasiparticle (QP) behavior. Here an extension of that work is provided by including the effect of the spin-orbit coupling on the Fermi-liquid regime of the layered ruthenates including applied magnetic fields. In the case of $Sr_3Ru_2O_7$ the main focus is on a many-body modeling that starts from the realistic low-symmetry band structure. Because of the fact that the MM problem involves very low energy scales in an underlying low-symmetry lattice, we believe that the bilayer system serves as a challenging test case for the reliability and accuracy of current extended-LDA approaches.

II. THEORETICAL APPROACH

The LDA part of this work is performed using an implementation[54] of the highly accurate mixed-basis pseudopotential (MBPP) technique,[55] employing norm-conserving pseudopotentials[56] and an efficient combined basis consisting of plane waves and additional localized orbitals. For the inclusion of spin-orbit coupling and to treat local many-body interactions, the realistic Hamiltonian

$$\mathcal{H} = \sum_{\mathbf{k}ijmm'\sigma} \varepsilon^{(\mathrm{ks})\prime}_{\mathbf{k}ijmm'} d^{\dagger}_{\mathbf{k}im\sigma} d_{\mathbf{k}jm'\sigma} + \sum_{\alpha} \mathcal{H}^{(\mathrm{loc})}_{\alpha} \tag{1}$$

is used, where $\mathbf{k}$ denotes the wave vector, α numbers the unit cells with i,j marking the Ru ions within, the spin-projection is given by $\sigma = \uparrow, \downarrow$, and $d^{(\dagger)}$ annihilates (creates) electrons in the t_{2g}-like Wannier orbitals m,m'. The Kohn-Sham dispersion $\boldsymbol{\varepsilon}_{\mathbf{k}}$ in the latter basis is here obtained from a maximally localized Wannier-function (MLWF) construction[57,58] based on the band structure revealed from the MBPP calculation. The prime in (1) indicates that strictly local (on-site) contributions are excluded in the k-dependent dispersion [see Eq. (3)]. More details on the determination of the dispersive part in the case of $Sr_3Ru_2O_7$, where the band Hamiltonian amounts to a 12×12 matrix due to the fact that the primitive unit cell encloses four Ru ions, is provided in Ref. 46. For Sr_2RuO_4 the primitive unit cell contains only one Ru ion and the Kohn-Sham problem asks for the diagonalization of a 3×3 matrix. The unit-cell Hamiltonian $\mathcal{H}^{(\mathrm{loc})}_{\alpha}$ decomposes into the four terms, reading

$$\mathcal{H}^{(\mathrm{loc})}_{\alpha} = \mathcal{H}^{(\mathrm{cf})}_{\alpha} + \mathcal{H}^{(\mathrm{soc})}_{\alpha} + \mathcal{H}^{(\mathrm{zm})}_{\alpha} + \mathcal{H}^{(\mathrm{int})}_{\alpha}, \tag{2}$$

and is evaluated in each particle sector of an effective t_{2g} problem. The first contribution includes the on-site crystal field through

$$\mathcal{H}^{(\mathrm{cf})}_{\alpha} = \sum_{imm'\sigma} \varepsilon^{(\mathrm{ks}),\mathrm{loc}}_{imm'} d^{\dagger}_{im\sigma} d_{im'\sigma}, \tag{3}$$

with $\varepsilon^{(\mathrm{ks}),\mathrm{loc}}_{imm'} = 1/N_{\mathbf{k}} \sum_{\mathbf{k}} \varepsilon^{(\mathrm{ks})}_{\mathbf{k}iimm'}$ computed from the complete Kohn-Sham dispersion. We continue with the spin-orbit interaction $\mathcal{H}^{(\mathrm{soc})}_{\alpha}$ of Russell-Saunders type (or LS coupling scheme) on each of the rather light Ru ions. Summing over the individual ion contributions leads to

$$\mathcal{H}^{(\mathrm{soc})}_{\alpha} = \lambda \sum_i \mathbf{L}_i \cdot \mathbf{S}_i = \frac{\lambda}{2} \sum_i \left(\mathbf{J}_i^2 - \mathbf{L}_i^2 - \mathbf{S}_i^2 \right), \tag{4}$$

where λ is the spin-orbit coupling parameter, $\mathbf{L}_i$ the total orbital momentum operator, $\mathbf{S}_i$ the total spin operator, and $\mathbf{J}_i = \mathbf{L}_i + \mathbf{S}_i$ the total angular momentum operator for each Ru ion, respectively. Note that in the Russell-Saunders approximation these three operators are true many-particle operators, given by the sum over the respective operators for each individual electron p within the t_{2g} shell, e.g., $\mathbf{L}_i = \sum_p \mathbf{L}_{ip}$ for the total orbital momentum operator. For the t_{2g} orbitals a valid choice for the matrix elements $\langle m|\mathbf{L}_{ip}|m'\rangle$ reads component-resolved[42]

$$L^x = \begin{pmatrix} 0 & 0 & \mathrm{i} \\ 0 & 0 & 0 \\ -\mathrm{i} & 0 & 0 \end{pmatrix}, \; L^y = \begin{pmatrix} 0 & 0 & 0 \\ 0 & 0 & -\mathrm{i} \\ 0 & \mathrm{i} & 0 \end{pmatrix}, \; L^z = \begin{pmatrix} 0 & -\mathrm{i} & 0 \\ \mathrm{i} & 0 & 0 \\ 0 & 0 & 0 \end{pmatrix}. \tag{5}$$

Due to the cubic crystal-field terms in the ruthenates, this representation is obtained by truncating the appropriate matrix elements of a full $4d$ shell based on cubic harmonics to a pure t_{2g} shell including the states $4d_{xz}$, $4d_{yz}$, and $4d_{xy}$. Although there is some minor intermixing with the e_g states at low energy for $Sr_3Ru_2O_7$ (see Sec. III), that approximation proves to be adequate on the present level of the investigation.

The third contribution to Eq. (2) describes the local interaction of the Zeeman type with a magnetic field $\mathbf{H}$ and can be written as

$$\mathcal{H}^{(zm)}_{\alpha} = \mu_{\mathrm{B}} \sum_i (\mathbf{L}_i + 2\mathbf{S}_i) \cdot \mathbf{H}. \tag{6}$$

Notice that in the weak-coupling regime $|\mathbf{H}| \ll \lambda$ considered in our calculations, the spin-orbit coupling dominates the magnetic-field interaction. Thus eigenvalues of L_z and S_z are no good quantum numbers of the system, but $\{J^2, J_z\}$ are now commuting with $\mathcal{H}^{(\mathrm{loc})}_{\alpha}$. Therefore we have to perform the projection of $\mathbf{L}_i$, $\mathbf{S}_i$ onto $\mathbf{J}_i$ according to the Wigner-Eckart theorem using the operators' common eigenspace representation. The term $\mathcal{H}^{(\mathrm{zm})}_{\alpha}$ has then the following form:

$$\begin{aligned} \mathcal{H}^{(zm)}_{\alpha} &= \mu_{\mathrm{B}} \sum_i \left(\frac{\langle \mathbf{L}_i \cdot \mathbf{J}_i \rangle_{LSJ}}{\langle J_i^2 \rangle_{LSJ}} + 2 \frac{\langle \mathbf{S}_i \cdot \mathbf{J}_i \rangle_{LSJ}}{\langle J_i^2 \rangle_{LSJ}} \right) \mathbf{J}_i \cdot \mathbf{H} \\ &= \mu_{\mathrm{B}} \sum_i \left(\frac{3}{2} + \frac{\langle S_i^2 \rangle_{LSJ} - \langle L_i^2 \rangle_{LSJ}}{2 \langle J_i^2 \rangle_{LSJ}} \right) \mathbf{J}_i \cdot \mathbf{H} \\ &= \mu_{\mathrm{B}} \sum_i \left(\frac{3}{2} + \frac{S(S+1) - L(L+1)}{2J(J+1)} \right) \mathbf{J}_i \cdot \mathbf{H} \\ &\equiv \mu_{\mathrm{B}} \sum_i g_i(LSJ) \, \mathbf{J}_i \cdot \mathbf{H}, \end{aligned} \tag{7}$$

where the notation $\langle \ldots \rangle_{LSJ}$ indicates the expectation value in that eigenspace defined by the eigenvalues of the operators L^2, S^2, and J^2, labeled by the quantum numbers L, S, and J, respectively.[59] Notably, the object $g_i(LSJ)$ is the generic matrix representation of the Landé factor (or g factor) in that eigenspace. After that eigenspace computation one has to transform $\mathcal{H}_\alpha^{(\mathrm{zm})}$ back into the original Hilbert space, where all other parts of the local Hamiltonian were derived. Note that in this way the g factor is calculated separately for each considered state.

Last but not least, Eq. (2) includes the electron-electron interaction $\mathcal{H}_\alpha^{(\mathrm{int})}$ provided by a multiorbital Hubbard model, which reads

$$\begin{aligned}\mathcal{H}_\alpha^{(\mathrm{int})} = U \sum_{im} n_{im\uparrow} n_{im\downarrow} + \frac{1}{2} \sum_{i,m\neq m',\sigma} \{ U' n_{im\sigma} n_{im'\bar{\sigma}} \\ + U'' n_{im\sigma} n_{im'\sigma} + J_{\mathrm{H}} d^\dagger_{im\sigma} d^\dagger_{im'\bar{\sigma}} d_{im\bar{\sigma}} d_{im'\sigma} \\ + J_{\mathrm{H}} d^\dagger_{im\sigma} d^\dagger_{im\bar{\sigma}} d_{im'\bar{\sigma}} d_{im'\sigma} \}\end{aligned} \tag{8}$$

with $n{=}d^\dagger d$. In Eq. (8) the first term marks the intraorbital Coulomb interaction with Hubbard U and the second term provides interorbital Hund's rule corrected interaction with $U' = U - J_{\mathrm{H}}$ and $U'' = U - 2J_{\mathrm{H}}$ for unequal and equal spin projections σ, respectively. The last two parts account for spin-flip and pair-hopping processes, vital to enforce the rotational invariance. These terms are especially important concerning the magnetic response of an interacting system.[52]

The complete Hamiltonian (1) embodies three interaction parameters, namely the spin-orbit interaction λ, the Hubbard U, and the Hund's exchange J_{H}. For both systems the value $\lambda = 0.09$ eV, as obtained from LDA calculations for Sr_2RuO_4 by Haverkort *et al.*,[30] is used for the SOC. Concerning the Coulomb interactions, previous works[25,26,29,31,47] located the Hubbard U for the layered ruthenates in the region 1.5–3.1 eV. Here we choose the moderate value $U = 2$ eV. With including SOC, that order of magnitude is sufficient to account for the key renormalization effects at low energy. The Hund's exchange is fixed to $J_{\mathrm{H}} = 0.35$ eV[25,26,31,60] throughout this work.

Our interacting ruthenate problem is solved via the rotationally invariant slave-boson (RISB) formalism[52,53] in the saddle-point approximation. It amounts to a decomposition of the electron's QP (fermionic $f_{\nu\sigma}$) and high-energy excitations (taken care of by the set of slave bosons $\{\phi\}$) on the operator level through $\underline{d}_{\nu\sigma} = \hat{R}[\{\phi\}]^{\sigma\sigma'}_{\nu\nu'} f_{\nu'\sigma'}$, where ν is a generic orbital/site index. Additional constraints for the normalization and to match the fermionic and bosonic contents are enforced on the mean-field level. The RISB electronic self-energy $\Sigma(\omega)$ at saddle-point is local and incorporates terms linear in frequency as well as static renormalizations. It is thus given by

$$\Sigma(\omega) = \omega(1 - \mathbf{Z}^{-1}) + \Sigma^{\mathrm{stat}}, \tag{9}$$

with

$$\Sigma^{\mathrm{stat}} = [\mathbf{R}^\dagger]^{-1} \Lambda \mathbf{R}^{-1} - \boldsymbol{\varepsilon}^{(\mathrm{ks}),\mathrm{loc}}, \tag{10}$$

whereby $\mathbf{Z}$ is the QP-weight matrix and Λ describes the matrix of Lagrange multipliers for the enforcement of the constraints. Expectation values of any given local operator $\mathcal{O}$ may be computed via the slave bosons according to

$$\langle \mathcal{O} \rangle = \sum_{AB} \langle A|\mathcal{O}|B\rangle \sum_q \phi^*_{Aq} \phi_{Bq}, \tag{11}$$

with A, B denoting atomic states and q as the QP index. For more details see Ref. 53. In the present scope the method may also be interpreted as a simplified approach to solve the dynamical mean-field theory (DMFT) equations (see, e.g., Ref. 61 for a review), compared to, e.g., more elaborate quantum Monte Carlo (QMC) techniques. Since we are interested in the low-energy physics of the layered ruthenates at rather small temperatures (where QMC usually becomes very challenging), this approach is thus well suited to access the Fermi-liquid regime including its extension to magnetically ordered phases.

III. CORRELATED ELECTRONIC STRUCTURE OF THE n=1,2 COMPOUNDS

Let us start by picturing the interacting electronic systems within Sr_2RuO_4 and $Sr_3Ru_2O_7$ at equilibrium for $\mathbf{H} = 0$. Besides the different number of Ru ions in the primitive unit cell, there are important differences in the crystal symmetry (see Fig. 1). The $n = 1$ compound has ideal tetragonal symmetry (space group $I4/mmm$) with the fourfold rotation C_4^z around the c axis. On the contrary, the $n = 2$ ruthenate shows orthorhombic symmetry (space group $Bbcb$), whereby the RuO_6 octahedra display a small rotation of 6.8° in the ab plane,[62] resulting only in the twofold symmetry element C_2^z. Basic structural and electronic differences may also be understood from a $\sqrt{2}\times\sqrt{2}$ reconstruction of the Sr_2RuO_4 unit cell within the ab plane.

Figure 2 depicts the band structure and the local Ru($4d$) density of states (DOS) of the two-layered compounds as

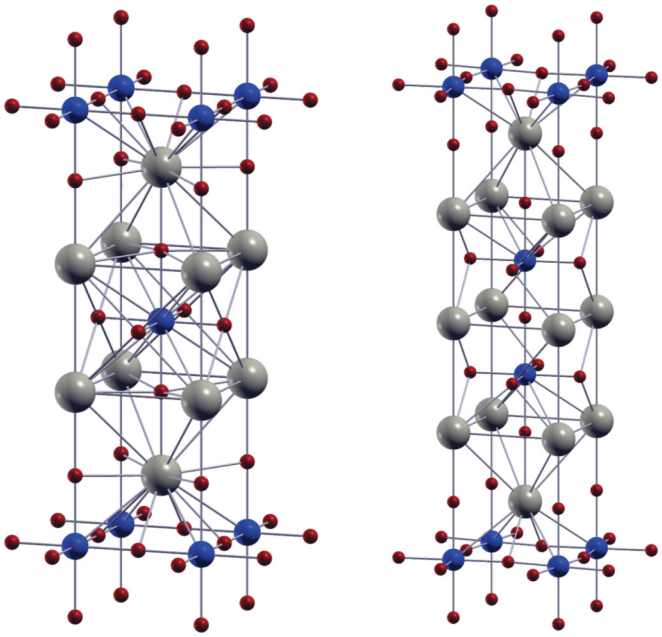

FIG. 1. (Color online) Crystal structures of Sr_2RuO_4 (left) and $Sr_3Ru_2O_7$ (right). Large gray: Sr, blue (dark): Ru, and small red (dark): O.

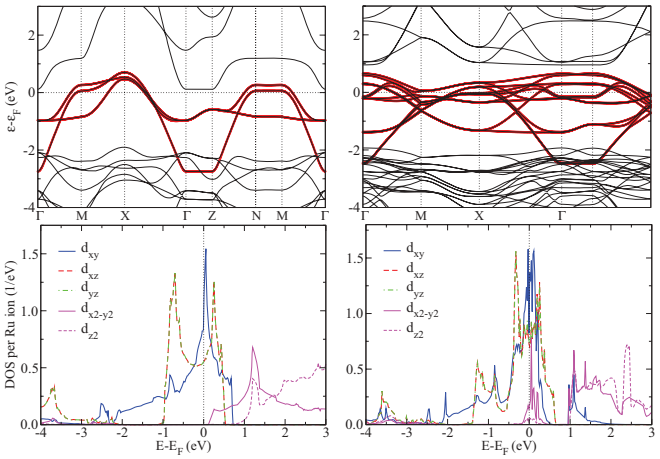

FIG. 2. (Color online) Comparison of band structure (top) and local Ru(4*d*) DOS (bottom) on the LDA level between Sr_2RuO_4 (left) and $Sr_3Ru_2O_7$ (right) when neglecting SOC. The red curves in the top pictures display the Wannier-like dispersion as obtained from the MLWF scheme. The angular-momentum resolution is obtained from projecting the Bloch states onto cubic harmonics with a radial extension of 2.0 a.u.

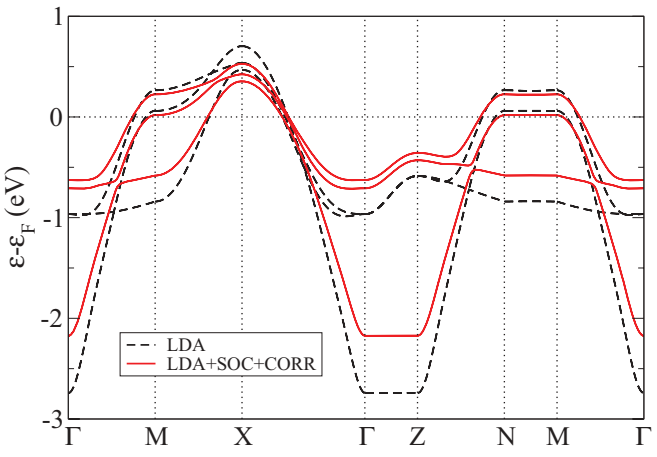

FIG. 3. (Color online) Sr_2RuO_4 quasiparticle band structure within standard LDA as well as with including SOC and correlations.

retrieved from conventional LDA calculations without SOC. The low-energy regime is dominated by the t_{2g} manifold of the Ru(4*d*) shell and can be downfolded to associated Wannier-like states. In both systems the latter leak into the oxygen-dominated block of bands. The overall t_{2g} bandwidth of the bilayer compound is slightly smaller (∼3.1 eV) than for the single-layer system (∼3.4 eV). The e_g contribution close to the Fermi level is minor for Sr_2RuO_4; however the $d_{x^2-y^2}$ character is nonnegligible close to ε_F for $Sr_3Ru_2O_7$,[16] as may be seen from the local DOS. Note that this contribution is included in the effective t_{2g}-MLWF construction.[46] In this respect it is important to record that we use in the following the (xy, xz, yz) terminology, though the corresponding orbitals are only t_{2g}-like in the sense of the present minimal MLWF construction. Note that these orbital functions (as true low-energy states) are pointing in between the Ru-O-Ru bonds of the in-plane square lattice (compare also Fig. 9).

In the single-layer compound the energetics of the t_{2g} manifold is split into (d_{xz}, d_{yz}) and d_{xy}. The d_{xz}, d_{yz} orbitals are truly degenerate, with crystal-field splitting $\Delta_{xy} = \varepsilon_{xz,yz} - \varepsilon_{xy} = 113$ meV to the d_{xy} Wannier level. With very small quantitative differences, $Sr_3Ru_2O_7$ has quasidegenerate d_{xz}, d_{yz} levels ($\Delta = 0.3$ meV) and $\Delta_{xy} = 115$ meV. Hence it has to be emphasized that there is already a small but nonzero splitting between d_{xz} and d_{yz}, giving rise to nominally slightly different local occupations. Note also that the strong local-DOS differentiation between (xz, yz) and xy no longer holds in the bilayer compound. Albeit the d_{xy} Wannier level is always lower in energy, the local orbital electron fillings in LDA for (d_{xy},d_{xz},d_{yz}) are (1.24, 1.38, 1.38) in the case of $n = 1$ and (1.40, 1.30, 1.30) for $n = 2$. Thus there is a change in the t_{2g} occupation hierarchy between both ruthenates due to band-dispersion effects. Right at the Fermi level, the DOS of Sr_2RuO_4 is close to a van Hove singularity slightly above ε_F, while in the case of the bilayer the Fermi level is located in a large dip of a complicated multi-valley-peak DOS at low energy.

Solving the problem posed by the minimal Hamiltonian (1) for each system results in modifications in the low-energy dispersions. Figure 3 shows the t_{2g}-like QP band structure of Sr_2RuO_4 from the extended-LDA treatment. One observes the expected combined main features already known from the existing separate SOC[28,30,32] and correlated[26,29,31,47] studies, namely the lifting of degeneracies, e.g., close to the Γ point for the bands with dominant xz, yz character, also resulting in now avoided band crossings, e.g., close to the X point, when including SOC. Electronic correlations lead in the present approximation to band-narrowing and -shifting. Lifetime effects as well as incoherent spectral weight cannot be retrieved within RISB at saddle point. But the method captures very well the slightly modified Fermi-level band crossings in, e.g., the ΓM direction as well as the shift of the van Hove singularity towards the M point.[14,15,26] The band renormalizations are substantial, however not quite as strong as obtained within DMFT calculations with more elaborate frequency dependence of the self-energy[26,29,31] to match the ARPES measurements. In the present modeling quantum fluctuations are missing and to obtain a ratio m^*/m_{LDA} of the order of 3–4 for Sr_2RuO_4, in good comparison with photoemission[15] and dHvA[12] data, a value $U > 3$ eV would be needed.

Accordingly, Fig. 4 depicts the comparison between the quasiparticle bands (including SOC and correlations) with the conventional LDA dispersions for the bilayer $Sr_3Ru_2O_7$. Due to the reduced symmetry the level of complexity is now surely raised. The complicated low-energy manifold with its rather flat bands already on the LDA level now shows significant effective-mass renormalization and additional splittings within the extended electronic structure examination. From experiment,[16,63] the ratio m^*/m_{LDA} is effectively on the order of 6, thus even larger than in the single-layer compound. Most interestingly, the blow-up of the computed Fermi-level neighborhood renders it obvious that especially close to the X point severe changes take place. For instance a twofold band approaching from M and splitting when passing X is strongly shifted to a low energy of about 7 meV in the occupied part.

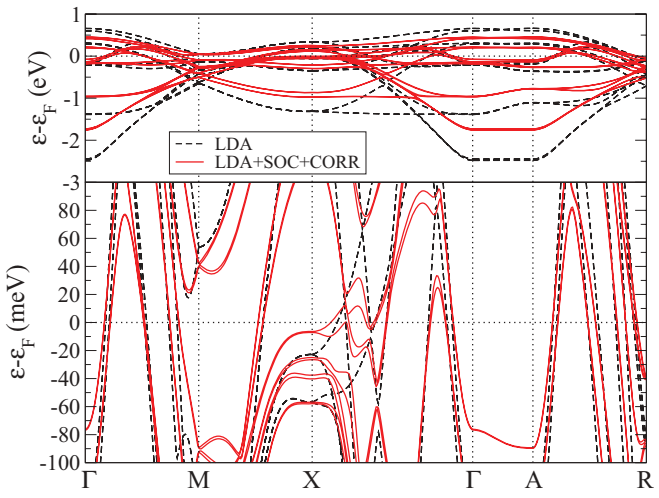

FIG. 4. (Color online) Same as Fig. 3, here for $Sr_3Ru_2O_7$. The lower panel provides a blow-up of the dispersions close to the Fermi level.

Importantly, the latter small scale may only be reached by the combination of SOC *and* explicit Coulomb interactions. While the spin-orbit coupling is responsible for the appearance of split-up bands, the electronic correlations provide the narrowing and further shifting towards ε_F. Increasing U and J_H leads to an even closer placement near the Fermi level (see Table I). Hence the present approach is truly capable of describing the very low energy scale the bilayer compound is famously known for. Furthermore the key features of the named dispersive structure around X with its local minima and maxima are in close agreement with results from ARPES studies by Tamai *et al.*[16] The Fermi-level crossings in this region of the Brillouin zone (BZ) give rise to the so-called γ_2 pocket, which is under strong suspicion to play a vital role in the peculiar metamagnetic behavior of this compound.[45] The complete Fermi surface (FS) obtained from our extended-LDA calculations exhibited in Fig. 5 is in good accordance with the one determined from photoemission.[16] However from our study the C_2^z-symmetry character seems vital in the fermiology, but note that the experimental data in Ref. 16 are symmetrized along the ΓX direction.

An important question concerns the band characters at low energy in order to touch base with the local-orbital viewpoint. Figure 6 therefore shows the so-called fat bands (orbital weight proportional to an artificial band broadening) for the t_{2g} manifold. Its easily seen that the bilayer system is far from being a textbook example when it comes to attributing bands to a certain azimuthal quantum numbers,

TABLE I. Energy (in meV) of the highest occupied band at the X point in $Sr_3Ru_2O_7$ for different U and J_H combinations (both in eV). In LDA without spin-orbit coupling that energy amounts to -22.8 meV.

	$J_H = 0.20$	$J_H = 0.35$	$J_H = 0.50$
$U = 1.5$	-13.9	-7.8	-4.4
$U = 2.0$	-13.6	-6.5	-2.8
$U = 2.5$	-11.1	-3.8	-0.6

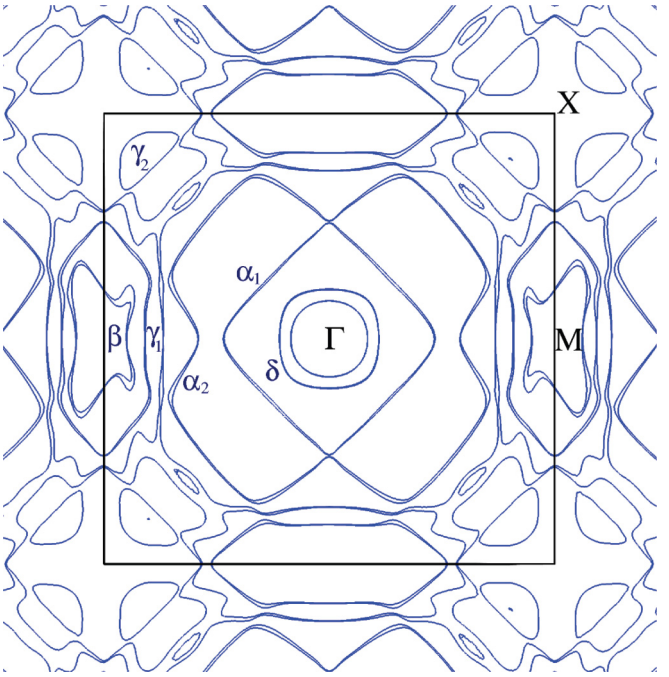

FIG. 5. (Color online) Interacting Fermi surface for $Sr_3Ru_2O_7$ in the basal $k_z = 0$ plane from extended LDA including SOC and electronic correlations. The black square marks the BZ cut and the labeling of the different sheets is according to Ref. 16.

since, e.g., the supposedly relevant bands close to X are of strong mixed t_{2g} character. Nonetheless small asymmetries may be identified. The topmost occupied band at X has

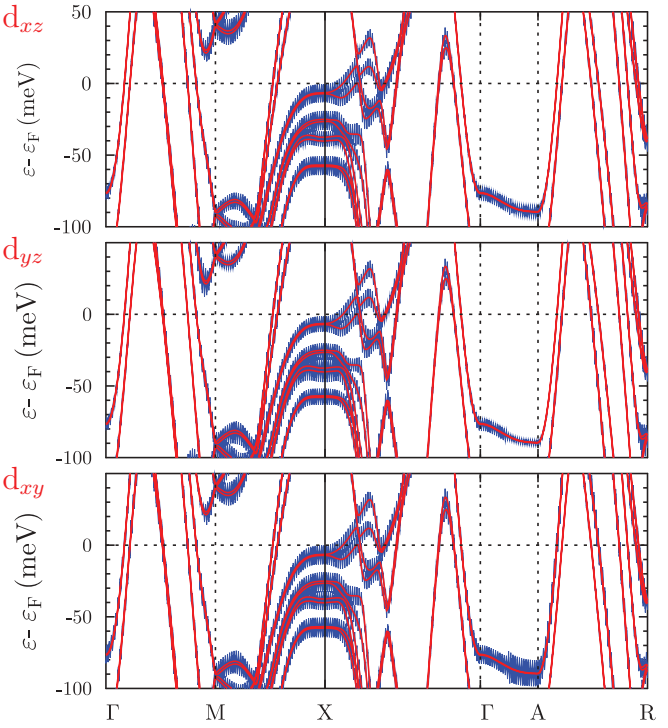

FIG. 6. (Color online) Individual weights of the t_{2g} Wannier orbitals on the low-energy QP bands from the extended-LDA calculation.

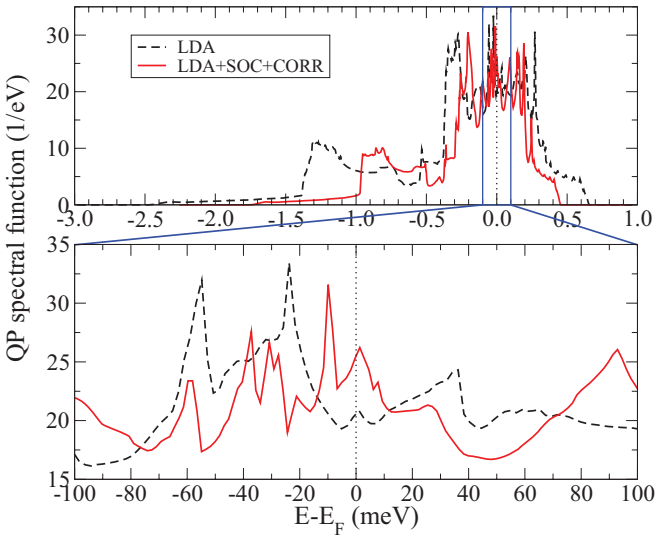

FIG. 7. (Color online) Interacting quasiparticle DOS for $Sr_3Ru_2O_7$ compared to the LDA result. The QP content including SOC and correlations is scaled with $Z = 0.7$ to account for the modified integrated spectral weight resulting from the slave-boson framework. The bottom panel shows a blow-up around the Fermi energy.

somewhat more d_{xz} than d_{yz} weight, true also for the lowest one in the given energy window. In between there is only one with more d_{yz} character. The d_{xy} orbital has notably overall the same order of weight in this region of the BZ as its out-of-plane companions. Interestingly, from the strong weight along ΓA the d_{xy} character seems to dominate the propagation perpendicular to the RuO_6 planes.

The low-energy scales may also be confirmed from the quasiparticle DOS plotted in Fig. 7. Therefrom it is again obvious that the states close to ε_F are strongly pronounced in extended LDA, shifting prominently to the Fermi energy. The LDA DOS exhibits a smaller peak at the Fermi level within a valley of ∼60 meV width. With the additional interactions that feature is strengthened and importantly a peak in the low-energy occupied region is sharpened and shifted towards ε_F, being located at ∼10 meV. These findings of increased spectral weight below ε_F within a meV range is in accordance with photoemission studies[16] and also supported from specific-heat data.[64]

Finally, Fig. 8 depicts the occupation probabilities of the local t_{2g}-based multiplets according to the converged slave-boson amplitudes of the lattice calculation in the metallic state. There are various sizable multiplet weights, not surprisingly with an overall domination of the ones from the four-particle sector. The atomic ground-state multiplet with $L = S = J = 1$, an orbital and spin triplet, has also the largest weight in the itinerant regime. Note that the deviations of J from the ideal values results from the small e_g weight intermixing within the LDA-derived Kohn-Sham Hamiltonian based on the low-energy t_{2g}-like orbitals. For Sr_2RuO_4 the corresponding picture looks very similar; also there the $L = S = J = 1$ multiplet has the maximum weight.

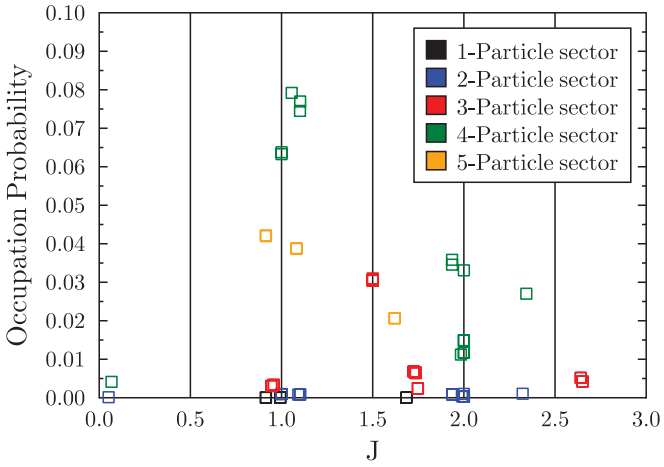

FIG. 8. (Color online) Histogram showing the occupation probabilities of calculated multiplets in $Sr_3Ru_2O_7$ ordered by the total angular momentum J.

IV. BILAYER RUTHENATE IN APPLIED MAGNETIC FIELD

Since our approach is in the position to correctly address the equilibrium low-energy correlated electronic structure, we expect a qualitatively meaningful description of $Sr_3Ru_2O_7$ with applied magnetic field **H**. The Zeeman-type local interaction is now included together with the spin-orbit and Coulomb interactions. All are adequately treated due to the generality of our formalism, also allowing for arbitrary field directions. Note that the crystal structure is constructed such that the in-plane square lattice evolves along the Ru-O-Ru bonds, while the original x, y axes point in between these bonding directions (see Fig. 9). In the present investigation the field direction is modified within the xz plane; i.e., the tilting of H takes place along the diagonal of the square lattice which also agrees with the orthorhombic a axis. Notably the x direction in real space corresponds to the $\Gamma M'$ (M rotated by 90°) direction in reciprocal space and therewith the $\Gamma X(X')$ direction amounts to QP propagation along the Ru-O-Ru bond on the rods of the square lattice. The resulting net magnetic moment M per Ru ion is composed of spin and orbital-momentum parts, i.e.,

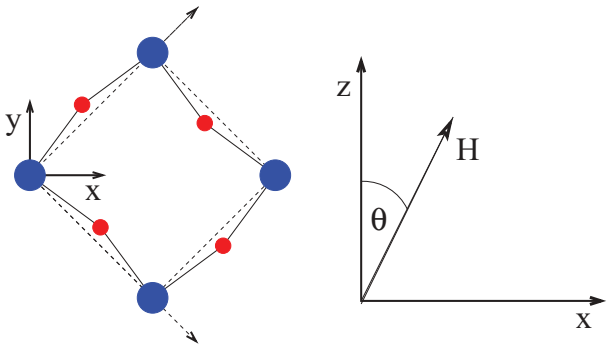

FIG. 9. (Color online) Left: View along the c axis of sketched $Sr_3Ru_2O_7$ in order to clarify the invoked Cartesian coordinate system with Ru ions in blue/dark and O ions in red/gray. Right: Applied magnetic field direction where the z axis equals the crystallographic c axis.

$M = \mu_B \langle g\, \mathbf{J} \cdot \mathbf{H} \rangle$, and is here computed on the local level from the self-consistent slave-boson amplitudes [see Eq. (11)] and not from k-integrating the associated QP contributions. While in effective single-particle calculations both approaches would yield identical results, in slave-boson theory those numbers may in principle differ since the QP part only carries the contribution to the itinerant character of the electron. Via Eq. (11) it is ensured that the occupation number of the physical electron is retrieved.

Because of the low-energy scales involved in this problem, especially for the close-to-realistic investigation of the magnetic behavior the numerics is however in any case far from simple. The complicated local interacting Hamiltonian asks for about 2000 slave-boson amplitudes to solve for, interlinked with a 24×24 QP-Hamiltonian problem (four Ru ions with three orbitals per ion, allowing for spin degrees of freedom within each orbital) on a properly dense k-point mesh.

A. The case H ∥ c

We first choose the crystallographic c axis (i.e., the z direction) perpendicular to the RuO_2 planes for the magnetic-field direction, i.e., $\mathbf{H} = H\hat{\mathbf{c}}$. Figure 10 shows the evolution of M with increasing field strength together with the obtained total free energy for the bilayer system. Both curves display a rather nontrivial behavior. In the following the values of H are given in meV. Up to $H = 5$ the value of M rises linearly (region I), with however negative free-energy curvature, hinting towards unfavorable field penetration. In the range $5 \lesssim H \lesssim 23$ a stronger rise of M occurs, followed by a nonmonotonic behavior (region II). In that second region the free energy is first depleting and then again rising along with the nonmonotonic part, overall evolving with the positive curvature of a stable phase. Let us also note that it appears as if in the first part $5 \lesssim H \lesssim 10$ the M evolution as well as the free-energy curve display some nontrivial modulation. Finally for even larger H (region III) the magnetic moment enhances further with close-to-linear development. In III the free energy follows a novel parabolic shape at higher values than in II. The described evolution reveals the metamagnetic behavior of M,

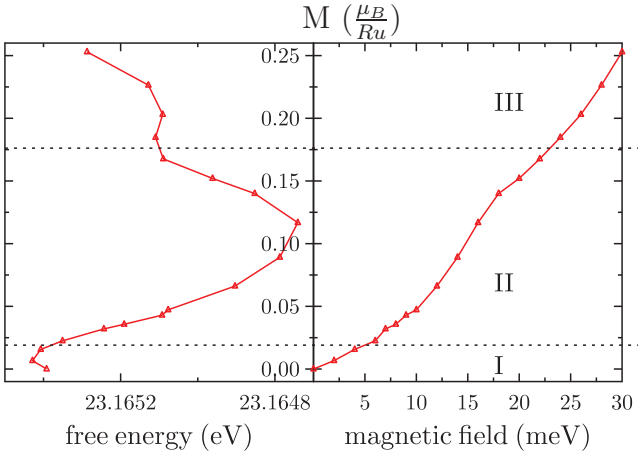

FIG. 10. (Color online) $Sr_3Ru_2O_7$ in applied magnetic field (measured in meV) along **z**. Left: Free energy vs net magnetic moment, right: net magnetic moment per Ru ion.

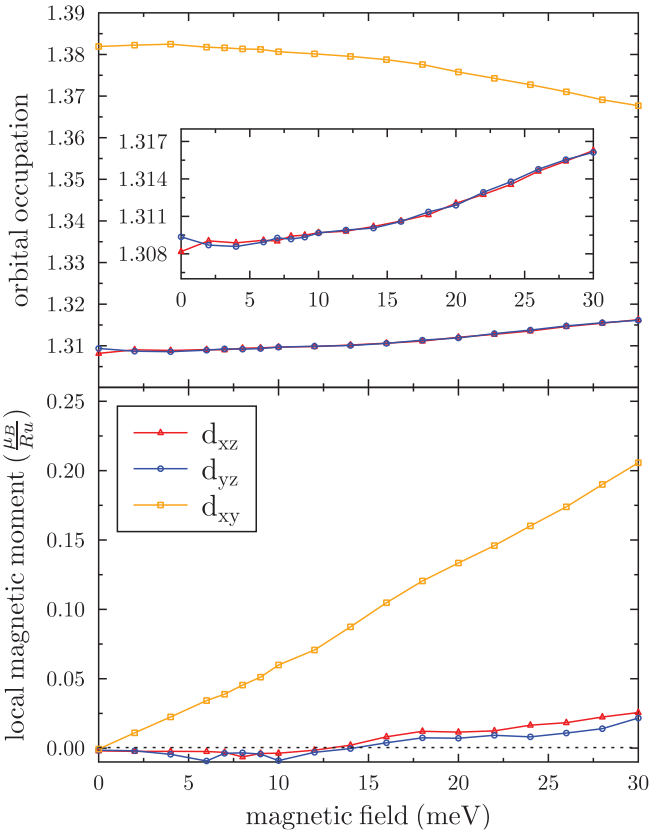

FIG. 11. (Color online) Orbital-resolved local occupation (top) and contributions to the Ru net magnetic moment (bottom) with magnetic field. The inset shows a blow-up of the d_{xz}, d_{yz} curves.

with strong resemblance to the experimental data.[20,21] Notably, the observed metamagnetism is again only obtained in the present computations if both, SOC *and* electronic correlations, are included. Due to the strong signatures in the free energy, the transition between regions I/II as well as regions II/III are clearly of first order. We however did not investigate the transition orders in a more elaborate fashion (e.g., via computing the Hesse matrix).

To connect these global results to the orbital degrees of freedom, Fig. 11 depicts the orbital-resolved local occupations and contributions to the magnetic moment. With increasing field the d_{xy} filling shrinks, while the one for d_{xz}, d_{yz} grows. Thus notably there is an interorbital charge transfer from d_{xy} to d_{xz}, d_{yz} with magnetic field. Whereas for $H = 0$ a marginal filling difference between the latter orbitals is observed, with growing magnetic field the occupations of the quasidegenerate levels more or less align. The respective orbital contributions to the magnetic moment within the t_{2g} manifold are strongly varying. While the dominant d_{xy} part shows substantial paramagnetic response with field, the generally much smaller d_{xz}, d_{yz} terms exhibit intricate behavior. They start with flat, nearly constant minor diamagnetic response for small magnetic field and both only turn into weak paramagnetic characteristics at $H \sim 13$. Interestingly, this PM behavior shows small differences in the amplitude for d_{xz} and d_{yz} (with $M_{xz} > M_{yz}$), with even an observable sudden increase in that difference when the II/III transition occurs. As the

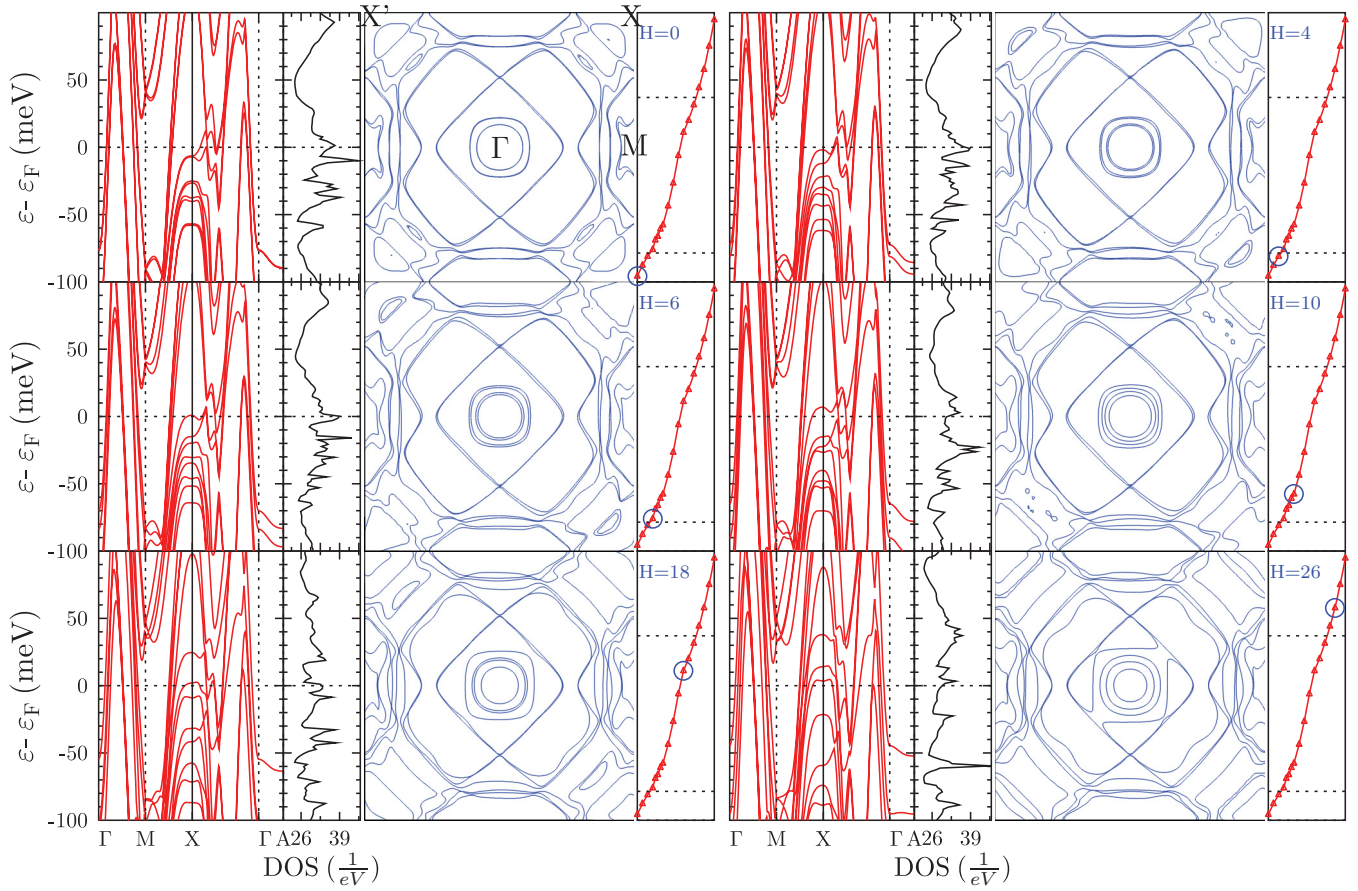

FIG. 12. (Color online) Development of the QP band structure, DOS, and Fermi surface with magnetic field along the z direction. The blue/gray circle on the right panel always marks the respective H value.

sole d_{xy} response shows no definite MM signals, the para/dia discrimination in the orbital response of d_{xz}, d_{yz} appears as a key microscopic building block for the MM behavior.

The orbital discrimination in the magnetic behavior already provides a first clue to the MM puzzle of the bilayer system. A second important insight originates from following the development of the QP bands with magnetic field, presented in Fig. 12. It is seen that increasing H amounts to intriguing changes in the low-energy manifold, most notably to relevant shifts in the peculiar QP structure close the X point. For $H = 4$, not surprisingly there are further band splittings along X compared to the case of zero magnetic field and the lowest-energy p-shaped band at this k-point is now placed just below ε_F. A discrimination between the γ_2 pockets around X and X' is furthermore clearly visible. Going to $H = 6$ the named band is locked to the Fermi level and γ_2 at X has opened towards the BZ boundary where as γ_2 at X' has shrunk. For $H = 10$ the former band is above ε_F and both γ_2 pockets are opened. At $H = 18$ the second-lowest band at X, X' crosses the Fermi level and a minor pocket structure reappears at X'. Moreover the α_2 sheet starts to become increasingly distorted along $\Gamma X(X')$ and also begins effectively shrinking with growing field. The latter signatures are strengthened for $H = 26$ with the additional onset of hybridization between α_1 and δ. The pockets close to X,X' remain both opened in that large-field region III, with now three low-energy bands having crossed ε_F at X,X'. Along with these changes, the QP DOS of course runs through several peaks at the Fermi energy, but evidently exhibiting an evolution different from a pure shifting of the $H = 0$ structure. Thus from the Bloch perspective the picture of Lifshitz transitions underlying the magnetic response emerges. Various authors have already pointed out the importance of van Hove singularities crossing the Fermi level and we here can verify this mechanism based on the complete realistic starting point. The fact that not only the γ_2 sheet but also the inner sheets, most notably α_2, may play a vital role in the MM response was also retrieved in a recent experimental study employing spectroscopic imaging scanning tunneling microscopy.[65]

The applied magnetic field leaves also some signatures in the orbital-dependent electronic self-energy (see Fig. 13). All orbital sectors display the expected splitting in the QP weight Z and static self-energy Σ^{stat} due to the spin-filling in balance with larger magnetic polarization. The splitting for d_{xz}, d_{yz} is weaker and especially minor at small field where the nearly constant diamagnetic response occurs. Overall there is no strong modification of the correlation strength with H; the MM signatures show up somewhat stronger in the QP weight that is associated with band renormalizations. From the calculation, the value for Z_{xy} is slightly larger than for the remaining two t_{2g} orbitals. But because of the intriguing hybridizations (compare Fig. 6) no trivial relation may be drawn therefrom

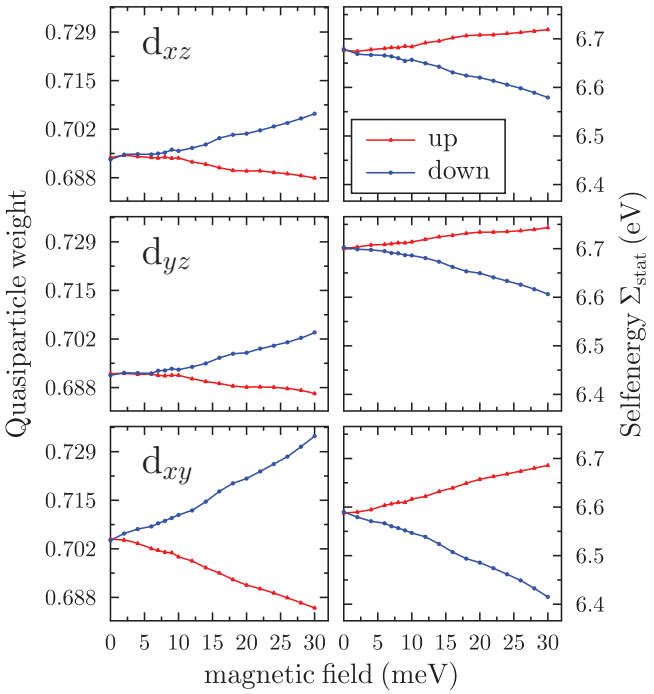

FIG. 13. (Color online) Orbital-dependent QP weight (right) and static self-energy (left) with H.

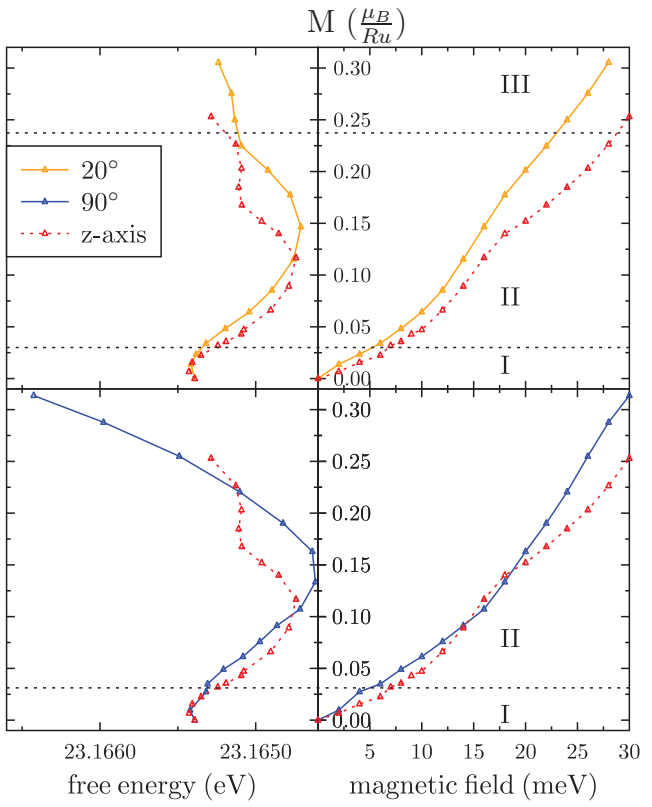

FIG. 15. (Color online) Free energies (left) and net magnetic moment (right) for $\theta = 20^\circ$ (top) and $\theta = 90^\circ$ (bottom), compared to the moment for H along the z direction ($\theta = 0^\circ$), respectively.

in view of the respective renormalized effective masses on the various Fermi sheets. Our RISB formalism is furthermore able to reveal the local-multiplet behavior of the correlated system. Via the slave-boson amplitudes the method allows us to evaluate the occupation probability of a given eigenstate of the local Hamiltonian (2) within the complete itinerant solution. For instance, Fig. 14 depicts the splitting characteristics of the ${}^4S_{3/2}$ multiplet from the three-particle sector associated with orbital momentum $L = 0$, i.e., having **J** as purely spin defined. As expected, the J_z degeneracy is lifted for $H \neq 0$, showing nontrivial signature close to the phase transitions between the different regions I–III. Sure enough, the four-particle sector is most dominantly occupied for the Ru($4d$) t_{2g} shell, but the multiplets there do not exhibit a very conclusive behavior with applied H.

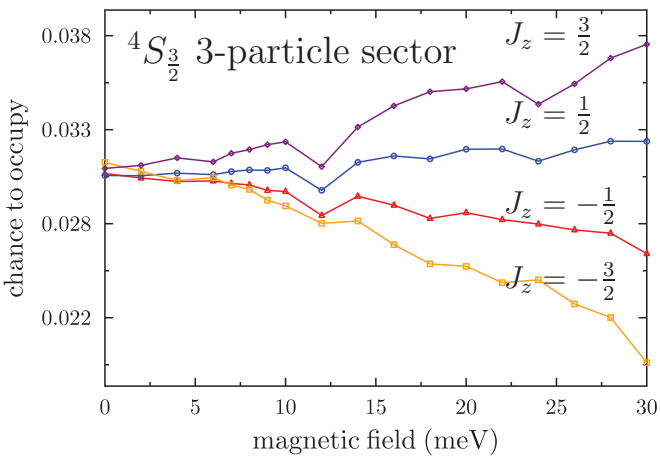

FIG. 14. (Color online) Splitting of the ${}^4S_{3/2}$ multiplet in the applied field.

B. The case H ∦ c

In principle our approach works for arbitrary polar angles θ between **H** and the c axis of the system. However since the computations are rather expensive we have chosen here

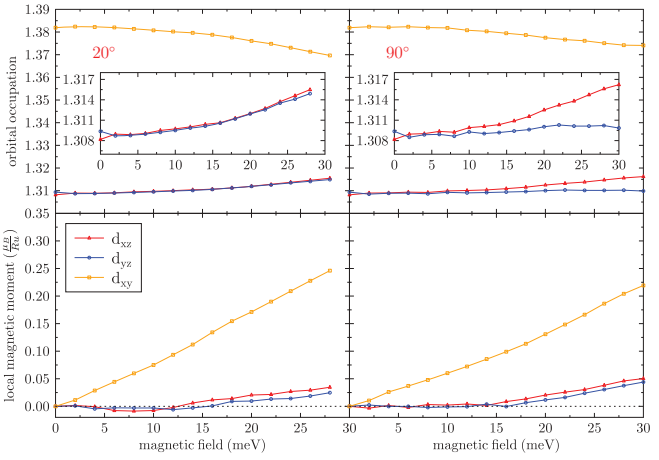

FIG. 16. (Color online) Orbital-resolved occupation and contributions to the magnetic moment as in Fig. 11, here for $\theta = 20^\circ$ (left) and $\theta = 90^\circ$ (right).

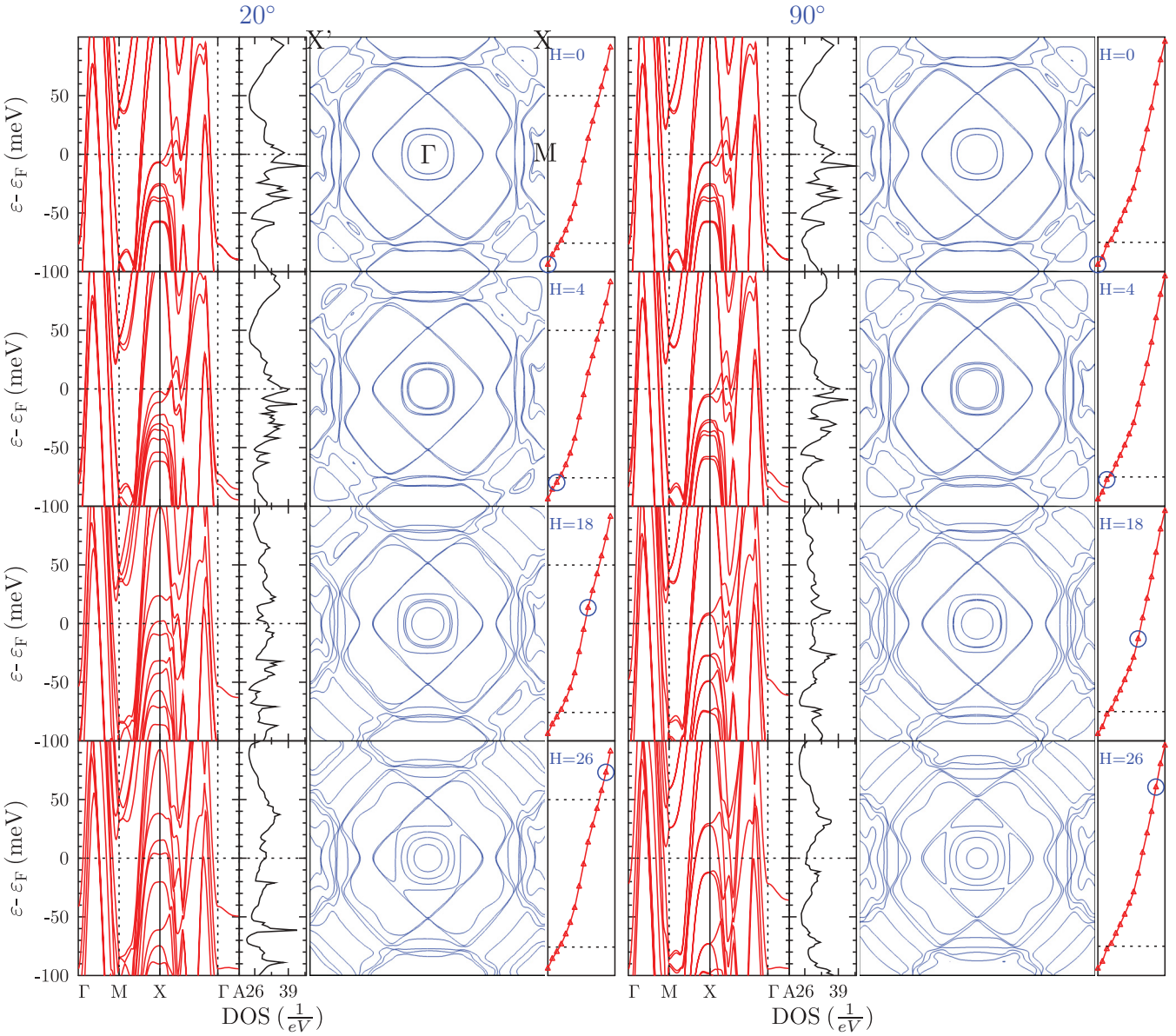

FIG. 17. (Color online) As Fig. 12, here for $\theta = 20^\circ$ (left) and $\theta = 90^\circ$ (right).

only two additional specific values (besides $\theta = 0$), namely $\theta = 20^\circ$ and $\theta = 90^\circ$. The azimuthal angle is put to zero; i.e., the latter in-plane magnetic field points along the x direction in between the Ru-O-Ru bond of the square lattice (see Fig. 9). The evolution of the net magnetic moment per Ru ion for the two new field angles together with the respective free-energy plot is displayed in Fig. 15. When directly comparing the magnetizations for $\theta = 20^\circ$ with the former $\theta = 0$, one first realizes that for a given H the value of M is increased. This seems to be in line with the experimental data from the work of Grigera *et al.*[22] showing an enhancement of the real part of the differential susceptibility at the MM transition with θ (note that θ is defined as the angle between field and the ab plane in Ref. 22). The overall phenomenology of $M(H)$ for $\theta = 20^\circ$ is still rather similar to the case $\mathbf{H}\|\mathbf{c}$. Note that although the upper first-order transition happens at larger magnetic moment for $\theta = 20^\circ$, the value corresponds to nearly the same magnetic-field strength H. On the contrary, for $\mathbf{H} \perp \mathbf{c}$ along x the overall characteristic is qualitatively different. After a near linear rise for $H > 5$, close to $H = 16$ a sudden change of slope for $M(H)$ takes place (with a possible signature in the free energy) and the magnetic moment continues again nearly linearly. The upper first-order transition is not visible anymore in the free-energy curve. This observation shows clear resemblance to the experimental findings of singular behavior for in-plane magnetic field compared to strong out-of-plane H.[11] However from the present computations we cannot draw a definite conclusion concerning the shift of the phase boundaries with respect to H and θ. We are nevertheless in the position to shed more light on the angular-dependent differences by showing in Fig. 16 the orbital contributions to the occupation and the magnetic moment for $\theta = 20^\circ$, 90°. For the smaller θ the orbital-resolved differences compared to H along c are marginal, with mainly an obvious occupation

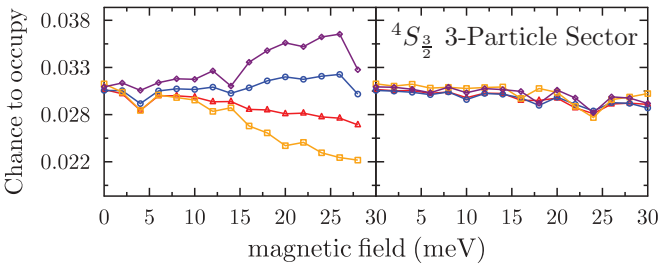

FIG. 18. (Color online) Splitting of the $^4S_{3/2}$ multiplet for $\theta = 20^\circ$ (left) and deferred splitting for $\theta = 90^\circ$ (right).

difference between d_{xz}, d_{yz} (with $n_{xz} > n_{yz}$) for $H > 22$ which was absent before. Comparing the results for H along x to the case along z shows again clear signature. The stronger occupation of d_{xz} occurs at already small magnetic field and becomes substantial at large H. Furthermore the former area of diamagnetic response from d_{xz}, d_{yz} has nearly vanished; both orbital responses are nearly indistinguishable from zero within the accuracy for small H. Yet at least for $H > 15$ the PM response with different amplitude is clearly observable. Thus the dia/para competition in d_{xz}, d_{yz} that seemed to be crucial for the MM behavior for H along z is nearly absent, explaining the qualitative difference between in- and out-of-plane field. Coming back to the phase-region shift with field and angle, and fixing such a shift to the dia/para crossing for d_{xz}, d_{yz}, one might observe that this crossing indeed shifts to the left, i.e., towards smaller H. However again the resolution is not accurate enough to render a unique statement concerning that question. The impact of the finite angle θ shows also up in the changes of the QP states with H, as documented in Fig. 17. While again for $\theta = 20^\circ$ there are no major qualitative differences compared to the case of H along c (e.g., also here the three low-lying bands at X cross the Fermi level with field), the pure in-plane field leads to clear modifications. Namely, the two originally nearly degenerate lowest-energy bands at X do *not* split with H, but cross ε_F together. In line with this, the four γ_2 pockets in the BZ behave coherently for all field strengths and also the δ-α_1 hybridization at large H occurs now in a fourfold manner. Importantly the third low-energy band (now also still degenerate with the fourth one) remains below the Fermi level within the range of the studied magnetic field. Thus H along the x axis leads to an avoided lifting of degeneracies, resulting in qualitative different magnetic response. However note that this on the other hand does not imply that the symmetry between d_{xz}, d_{yz} is enforced, since the local orbital discrepancy is strongly *increased* for the sole in-plane field (compare Fig. 16). Such selection-rule constraints depending on the magnetic-field direction show up also prominently when it comes to local-multiplet splittings, as shown in Fig. 18 for our example of the $L = 0$ $^4S_{3/2}$ many-body state from the three-particle sector. While the J_z splitting for $\theta = 20^\circ$ remains vital, in the case of H along x the splitting is mostly absent. For further clarification, Fig. 19 depicts the resulting angle between applied field and net magnetization, rendering it clear that only at large enough field strength the moment aligns along H. In this respect it appears as if for $\mathbf{H} \perp \mathbf{c}$ the moment is somewhat more easily forced into the field direction.

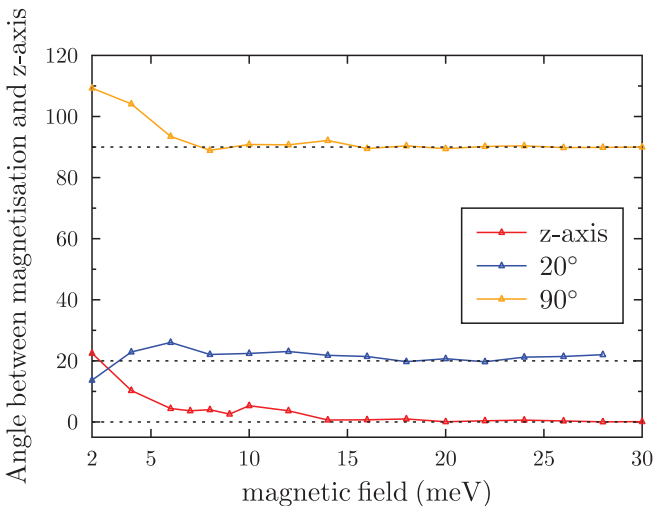

FIG. 19. (Color online) Angle between applied magnetic field H and resulting net magnetic Ru moment for $\theta = 0, 20^\circ, 90^\circ$.

V. SUMMARY AND DISCUSSION

The physical content of this work is twofold. First the interplay of spin-orbit coupling and local Coulomb interactions was studied at equilibrium for the $n = 1,2$ layered strontium ruthenium oxides belonging to the Ruddlesden-Popper family. Thereby we started from the realistic low-energy Kohn-Sham dispersion as obtained from Wannier-downfolding the bands from state-of-the-art LDA calculations. Then notably the multiorbital many-body effects (and its interlinking with spin-orbit effects) were treated beyond simple Hartree-Fock mean field by utilizing proper self-consistent renormalizations due to strong correlations within rotationally invariant slave-boson theory at saddle point.

For both compounds it became evident that SOC and strong correlations together are important to account for the detailed low-energy electronic structure at small temperatures. Already in Sr_2RuO_4 the local Coulomb correlations effectively renormalized the spin-orbit interaction, leading to enhanced band splittings for the t_{2g} manifold close to the Fermi level. Its is therefore surely expected that the unconventional superconductivity at low T has to be addressed by treating these both interaction types on equal footing.[33] For the bilayer compound $Sr_3Ru_2O_7$ such an approach was shown to be essential in order to describe the intriguing low-energy quasiparticle band structure and density of states in close resemblance to existing ARPES and specific-heat measurements.[16,64] The renormalized spin-orbit split bands give rise to extremely small energy scales, whereby close to the X point in the BZ an especially rich structure appears. However a straightforward decomposition of the complicated renormalized band structure into distinct d_{xy}-, d_{xz}-, or d_{yz}-like bands seems difficult; the system looks like an intricate multiorbital system where subtle differences in the orbital contributions eventually play a crucial role.

Beyond the equilibrium study, a straightforward examination of the bilayer ruthenate in applied magnetic field, based on the complete multiorbital t_{2g} Hamiltonian including the Zeeman term in the presence of SOC, was presented. Depending on the magnetic-field direction, metamagnetic

transitions in line with first-order phase transitions were verified. Taking a local viewpoint in that metallic system, the competition between paramagnetic (d_{xy}) and diamagnetic (d_{xz}, d_{yz}) contributions appears to play a significant role for the MM phenomena. Moreover an orbital charge transfer from d_{xy} to d_{xz}, d_{yz} with increasing H was observed, though the orbital fillings between the latter two t_{2g} orbitals only seem to deviate with larger field angle θ. Concerning the itinerant QP states it became evident that Lifshitz transitions close to the X point (i.e., around the γ_2 pocket) may partly be blamed for changes in the free energy and accompanying Fermi-surface reconstructions across the MM transitions. But moreover a substantial change of the α_2 sheet and an additional α_1-δ hybridization is seen with larger magnetic field. While the region around X corresponds to propagation along the Ru-O-Ru bond with strong short-range variation, the latter inner sheets account for rather isotropic in-plane transport with only long-range variation in the respective QP wave function. Thus the physics of the MM transitions involves directional, short-range processes at smaller H and incorporates long-range mechanisms at larger H. In addition, symmetry changes seem to take place between certain regions of the BZ. Albeit the overall C_2^z symmetry of the total FS remains stable with H, the original C_4^z-like symmetry between the γ_2 pockets is disturbed towards C_2^z in the central MM phase region II, if $\mathbf{H}||\mathbf{c}$ holds. However that symmetry change is absent for $\mathbf{H}\perp\mathbf{c}$ and a well-defined bounded MM region cannot be identified. Thus the present calculations reveal the qualitative differences between out-of-plane and in-plane magnetic field in accordance with experiment (see Ref. 11 for a recent review).

There remain however open questions. For instance, we may not draw definite conclusions on the shifting of the MM transitions with field angle, whereas in some model studies[40,44] the shift of the MM phase region to lower magnetic fields with θ in line with experimental work was verified. Besides several other possible reasons, this angle-dependent behavior might also be sensitive to the specific choice for the magnitude of the interaction parameters U, J_{H}, and λ within the local Hamiltonian, also in conjunction with the nesting properties between the various spin-polarized Fermi sheets.[44]

Another important point concerns the appearance of nematic order, revealed in transport studies for $Sr_3Ru_2O_7$ to escort the MM region.[66] We evidently see symmetry changes in the FS geometry and standard representations of nematic order parameters for a certain angular-momentum ordering channel l of the form $\mathcal{N}_l = \sum_{\mathbf{k}} n(\mathbf{k}) \exp[il\varphi(\mathbf{k})]$ (see, e.g., Ref. 67 for a review) display nontrivial behavior with H depending on l and on the number of included bands. However the computed data do not exhibit convincing evidence for a well-defined quantification of nematicity along that definition. Note that we also did not incorporate such a symmetry-breaking (i.e., forward-scattering) term explicitly in the Hamiltonian, as done in some model studies,[37,38,40,41,44] and it might therefore be possible that we miss additional (energetically favorable) symmetry breakings in our mean-field approach. For the present problem, the nematic order parameter has frequently also been defined via the filling difference between the d_{xz}, d_{yz} orbitals.[40,41] Yet this definition seems dangerous, since the C_2^z symmetry of $Sr_3Ru_2O_7$ is broken already by the equilibrium crystal structure and LDA calculations reveal such a nominal filling difference for $H = 0$. On the other hand our extended-LDA calculations point towards an initial alignment of these suborbital fillings with magnetic field. Only for larger (H, θ) a true d_{xz}, d_{yz} filling differentiation occurs. In this respect its also noteworthy that here the magnetic-field tilting towards the ab plane takes place in between the Ru-O-Ru bond, i.e., along the diagonal a axis of the in-plane square lattice. It would therefore be interesting to check further additional in-plane directions, especially along Ru-O-Ru.

This brings us to possible extensions of the current work on $Sr_3Ru_2O_7$. For present numerical reasons, the different Ru ions in the bilayer unit cell were assumed equivalent by symmetry (as true for the equilibrium crystal structure). But we easily expect that the MM phase regions would generally benefit from such a symmetry breaking within the unit cell. If orbital-liquid scenarios or the physics of domain structures[11,68] in the compound are vital, one has to come up with even more sophisticated real-space picturings. Intersite Coulomb interactions are here neglected, but may also be a source for the observed symmetry breakings.[45] Furthermore since this work was performed by using a postprocessing scheme to existing LDA calculations, elaborating on a complete charge-self-consistent approach with the proper feedback of the electronic self-energy onto the Kohn-Sham charge density could surely enhance the MM response. Accounting for finite-temperature effects is an additional further important aspect in order to reveal the intricate thermodynamics of the MM region.[69] Last but not least, at the moment the method relies on mean-field theory. Since in other strongly correlated materials it is already found that intricate self-energy effects especially take place close to van Hove singularities,[70] local quantum fluctuations should be included in future $Sr_3Ru_2O_7$ studies. Nonlocal quantum spin fluctuations may have relevant impact on the low-energy physics, since the material is prone to magnetic order. Nonetheless the present realistic formalism yields promising results and shows that extended-LDA calculations are in principle capable of addressing the challenging low-energy physics of the layered ruthenates.

ACKNOWLEDGMENTS

We thank D. Grieger for helpful discussions. Financial support from the Free and Hanseatic City of Hamburg in the context of the Landesexzellenzinitiative Hamburg as well as the DFG-FOR 1346 is gratefully acknowledged. Computations were performed at the local computing center of the University of Hamburg as well as the North-German Supercomputing Alliance (HLRN) under the grant hhp00026.

[1] R. J. Cava, Dalton Trans. **19**, 2979 (2004).
[2] Y. Maeno, H. Hashimoto, K. Yoshida, S. Nishizaki, T. Fujita, A. P. Mackenzie, J. G. Bednorz, and F. Lichtenberg, Nature (London) **372**, 532 (1994).
[3] T. M. Rice and M. Sigrist, J. Phys.: Condens. Matter **7**, L643 (1996).
[4] A. P. Mackenzie and Y. Maeno, Rev. Mod. Phys. **75**, 657 (2003).
[5] C. S. Alexander, G. Cao, V. Dobrosavljevic, S. McCall, J. E. Crow, E. Lochner, and R. P. Guertin, Phys. Rev. B **60**, 8422R (1999).

[6]E. Gorelov, M. Karolak, T. O. Wehling, F. Lechermann, A. I. Lichtenstein, and E. Pavarini, Phys. Rev. Lett. **104**, 226401 (2010).
[7]I. I. Mazin and D. J. Singh, Phys. Rev. Lett. **82**, 4324 (1999).
[8]Y. Sidis, M. Braden, P. Bourges, B. Hennion, S. NishiZaki, Y. Maeno, and Y. Mori, Phys. Rev. Lett. **83**, 3320 (1999).
[9]M. K. Crawford, R. L. Harlow, W. Marshall, Z. Li, G. Cao, R. L. Lindstrom, Q. Huang, and J. W. Lynn, Phys. Rev. B **65**, 214412 (2002).
[10]S.-I. Ikeda, Y. Maeno, S. Nakatsuji, M. Kosaka, and Y. Uwatoko, Phys. Rev. B **62**, 6089(R) (2000).
[11]A. P. Mackenzie, J. A. N. Bruin, R. A. Borzi, A. W. Rost, and S. A. Grigera, arXiv:1201.6639.
[12]A. P. Mackenzie, S. R. Julian, A. J. Diver, G. J. McMullan, M. P. Ray, G. G. Lonzarich, Y. Maeno, S. Nishizaki, and T. Fujita, Phys. Rev. Lett. **76**, 3786 (1996).
[13]T. Yokoya, A. Chainani, T. Takahashi, H. Katayama-Yoshida, M. Kasai, and Y. Tokura, Phys. Rev. Lett. **76**, 3009 (1996).
[14]A. Damascelli, D. H. Lu, K. M. Shen, N. P. Armitage, F. Ronning, D. L. Feng, C. Kim, Z.-X. Shen, T. Kimura, Y. Tokura, Z. Q. Mao, and Y. Maeno, Phys. Rev. Lett. **85**, 5194 (2000).
[15]K. M. Shen, A. Damascelli, D. H. Lu, N. P. Armitage, F. Ronning, D. L. Feng, C. Kim, Z.-X. Shen, D. J. Singh, I. I. Mazin, S. Nakatsuji, Z. Q. Mao, Y. Maeno, T. Kimura, and Y. Tokura, Phys. Rev. B **64**, 180502(R) (2001).
[16]A. Tamai, M. P. Allan, J. F. Mercure, W. Meevasana, R. Dunkel, D. H. Lu, R. S. Perry, A. P. Mackenzie, D. J. Singh, Z.-X. Shen, and F. Baumberger, Phys. Rev. Lett. **101**, 026407 (2008).
[17]C. Mirri, L. Baldassarre, S. Lupi, M. Ortolani, R. Fittipaldi, A. Vecchione, and P. Calvani, Phys. Rev. B **78**, 155132 (2008).
[18]Y. Maeno, K. Yoshida, H. Hashimoto, S. Nishizaki, S. Ikeda, M. Nohara, T. Fujita, A. P. Mackenzie, N. E. Hussey, J. G. Bednorz, and F. Lichtenberg, J. Phys. Soc. Jpn. **66**, 1405 (1997).
[19]Z. Qu, L. Spinu, H. Yuan, V. Dobrosavljević, W. Bao, J. W. Lynn, M. Nicklas, J. Peng, T. Liu, D. Fobes, E. Flesch, and Z. Q. Mao, Phys. Rev. B **78**, 180407(R) (2008).
[20]R. S. Perry, L. M. Galvin, S. A. Grigera, L. Capogna, A. J. Schofield, A. P. Mackenzie, M. Chiao, S. R. Julian, S. Ikeda, S. Nakatsuji, Y. Maeno, and C. Pfleiderer, Phys. Rev. Lett. **86**, 2661 (2001).
[21]A. W. Rost, R. S. Perry, J.-F. Mercure, A. P. Mackenzie, and S. A. Grigera, Science **325**, 1360 (2009).
[22]S. A. Grigera, R. A. Borzi, A. P. Mackenzie, S. R. Julian, R. S. Perry, and Y. Maeno, Phys. Rev. B **67**, 214427 (2003).
[23]P. Gegenwart, F. Weickert, M. Garst, R. S. Perry, and Y. Maeno, Phys. Rev. Lett. **96**, 136402 (2006).
[24]S. A. Grigera, R. S. Perry, A. J. Schofield, M. Chiao, S. R. Julian, G. G. Lonzarich, S. I. Ikeda, Y. Maeno, A. J. Millis, and A. P. Mackenzie, Science **294**, 329 (2001).
[25]M. Cuoco, C. Noce, and A. Romano, Phys. Rev. B **57**, 11989 (1998).
[26]A. Liebsch and A. Lichtenstein, Phys. Rev. Lett. **84**, 1591 (2000).
[27]J. Spalek, Phys. Rev. B **63**, 104513 (2001).
[28]E. Pavarini and I. I. Mazin, Phys. Rev. B **74**, 035115 (2006).
[29]Z. V. Pchelkina, I. A. Nekrasov, T. Pruschke, A. Sekiyama, S. Suga, V. I. Anisimov, and D. Vollhardt, Phys. Rev. B **75**, 035122 (2007).
[30]M. W. Haverkort, I. S. Elfimov, L. H. Tjeng, G. A. Sawatzky, and A. Damascelli, Phys. Rev. Lett. **101**, 026406 (2008).
[31]J. Mravlje, M. Aichhorn, T. Miyake, K. Haule, G. Kotliar, and A. Georges, Phys. Rev. Lett. **106**, 096401 (2011).
[32]E. J. Rozbicki, J. F. Annett, J.-R. Souquet, and A. P. Mackenzie, J. Phys.: Condens. Matter **23**, 094201 (2011).
[33]J. J. Deisz and T. E. Kidd, Phys. Rev. Lett. **107**, 277003 (2011).
[34]D. J. Singh and I. I. Mazin, Phys. Rev. B **63**, 165101 (2001).
[35]B. Binz and M. Sigrist, Europhys. Lett. **65**, 816 (2004).
[36]S. A. Grigera, P. Gegenwart, R. A. Borzi, F. Weickert, A. J. Schofield, R. S. Perry, T. Tayama, T. Sakakibara, Y. Maeno, A. G. Greena, and A. P. Mackenzie, Science **306**, 1154 (2004).
[37]H.-Y. Kee and Y. B. Kim, Phys. Rev. B **71**, 184402 (2005).
[38]C. M. Puetter, H. Doh, and H. Y. Kee, Phys. Rev. B **76**, 235112 (2007).
[39]A. M. Berridge, A. G. Green, S. A. Grigera, and B. D. Simons, Phys. Rev. Lett. **102**, 136404 (2009).
[40]S. Raghu, A. Paramekanti, E.-A. Kim, R. A. Borzi, S. A. Grigera, A. P. Mackenzie, and S. A. Kivelson, Phys. Rev. B **79**, 214402 (2009).
[41]W.-C. Lee and C. Wu, Phys. Rev. B **80**, 104438 (2009).
[42]W.-C. Lee, D. P. Arovas, and C. Wu, Phys. Rev. B **81**, 184403 (2010).
[43]W.-C. Lee and C. Wu, arXiv:1008.2486.
[44]M. H. Fischer and M. Sigrist, Phys. Rev. B **81**, 064435 (2010).
[45]C. M. Puetter, J. G. Rau, and H. Y. Kee, Phys. Rev. B **81**, 081105(R) (2010).
[46]C. Piefke and F. Lechermann, Phys. Status Solidi B **248**, 2269 (2011).
[47]M. Malvestuto, E. Carleschi, R. Fittipaldi, E. Gorelov, E. Pavarini, M. Cuoco, Y. Maeno, F. Parmigiani, and A. Vecchione, Phys. Rev. B **83**, 165121 (2011).
[48]S. E. Barnes, J. Phys. F.: Met. Phys. **6**, 1375 (1976).
[49]N. Read and D. M. Newns, J. Phys. C: Solid State Phys. **16**, 3273 (1983).
[50]P. Coleman, Phys. Rev. B **29**, 3035 (1984).
[51]G. Kotliar and A. E. Ruckenstein, Phys. Rev. Lett. **57**, 1362 (1986).
[52]T. Li, P. Wölfle, and P. J. Hirschfeld, Phys. Rev. B **40**, 6817 (1989).
[53]F. Lechermann, A. Georges, G. Kotliar, and O. Parcollet, Phys. Rev. B **76**, 155102 (2007).
[54]B. Meyer, C. Elsässer, F. Lechermann, and M. Fähnle, FORTRAN 90 Program for Mixed-Basis-Pseudopotential Calculations for Crystals, Max-Planck-Institut für Metallforschung, Stuttgart.
[55]S. G. Louie, K. M. Ho, and M. L. Cohen, Phys. Rev. B **19**, 1774 (1979).
[56]D. Vanderbilt, Phys. Rev. B **32**, 8412 (1985).
[57]N. Marzari and D. Vanderbilt, Phys. Rev. B **56**, 12847 (1997).
[58]I. Souza, N. Marzari, and D. Vanderbilt, Phys. Rev. B **65**, 035109 (2001).
[59]C. Cohen-Tannoudji, B. Diu, and F. Laloë, *Quantum Mechanics* Pt. 2, 3rd ed., Vol. 2 (Walter de Gruyter, Inc. Herndon, VA, USA, 2008).
[60]S. Okamoto and A. J. Millis, Phys. Rev. B **70**, 195120 (2004).
[61]A. Georges, G. Kotliar, W. Krauth, and M. J. Rozenberg, Rev. Mod. Phys. **68**, 13 (1996).
[62]H. Shaked, J. D. Jorgensen, O. Chmaissem, S. Ikeda, and Y. Maeno, J. Solid State Chem. **154**, 361 (2000).
[63]J.-F. Mercure, A. W. Rost, E. C. T. O'Farrell, S. K. Goh, R. S. Perry, M. L. Sutherland, S. A. Grigera, R. A. Borzi, P. Gegenwart, A. S. Gibbs, and A. P. Mackenzie, Phys. Rev. B **81**, 235103 (2010).
[64]A. W. Rost, A. M. Berridge, R. S. Perry, J.-F. Mercure, S. A. Grigera, and A. P. Mackenzie, Phys. Status Solidi B **247**, 513 (2010).

[65]J. Lee, M. P. Allan, M. A. Wang, J. Farrell, S. A. Grigera, F. Baumberger, J. C. Davis, and A. P. Mackenzie, Nat. Phys. **5**, 800 (2009).

[66]R. A. Borzi, S. A. Grigera, J. Farrell, R. S. Perry, S. J. S. Lister, S. L. Lee, D. A. Tennant, Y. Maeno, and A. P. Mackenzie, Science **315**, 214 (2006).

[67]E. Fradkin, S. A. Kivelson, M. J. Lawler, J. P. Eisenstein, and A. P. Mackenzie, Annu. Rev. Condens. Matter Phys. **1**, 153 (2010).

[68]C. Stingl, R. S. Perry, Y. Maeno, and P. Gegenwart, Phys. Rev. Lett. **107**, 026404 (2011).

[69]A. W. Rost, S. A. Grigera, J. A. N. Bruin, R. S. Perry, D. Tian, S. Raghu, S. A. Kivelson, and A. P. Mackenzie, Proc. Natl. Acad. Sci. USA **108**, 16549 (2011).

[70]O. E. Peil, A. Georges, and F. Lechermann, Phys. Rev. Lett. **107**, 236404 (2011).